Infrared Physics and Technology 103 (2019) 103044

Contents lists available at ScienceDirect

Infrared Physics & Technology

journal homepage: www.elsevier.com/locate/infrared

Health status detection of neonates using infrared thermography and deep convolutional neural networks

Ahmet Haydar Ornek[a], Murat Ceylan[a,*], Saim Ervural[b]

[a] Faculty of Engineering and Natural Sciences, The Department of Electrical and Electronics Engineering, Konya Technical University, Konya, Turkey
[b] Faculty of Engineering, The Department of Electrical and Electronics Engineering, KTO Karatay University, Konya, Turkey

ARTICLE INFO

Keywords:
Thermal imaging
Premature baby
Deep learning
Convolutional neural network
Classification

ABSTRACT

Protection of body temperature is critically important for health. Diseases and infections cause local temperature imbalances in the body. Infrared Thermography (IRT), which is a non-invasive and non-contact method, has been used in medical applications for decades. Pre-diagnosis and follow-up treatment systems can be realized by monitoring the temperature distribution in the body. In this study, IRT and deep Convolutional Neural Networks (CNNs) models were used together for the first time to detect the health status of neonates. Neonatal thermal images have been taken in the Neonatal Intensive Care Unit (NICU) of Selcuk University, Faculty of Medicine (Konya, Turkey), over a one-year period. Neonatal thermal images were obtained from selected 19 healthy and 19 unhealthy neonates. Data augmentation methods, such as brightness enhancement, color transformation, resolution and contrast changes, and the addition of different noises, were applied to the thermal images for the training of a CNN model. A number of 3800 thermal images taken from neonates in NICU were augmented to 15,200 and 30,400 thermal images. Then, using CNNs, 380, 3800, 15,200, and 30,400 neonatal thermal images were classified as healthy and unhealthy. The optimal result obtained was with 99.58% accuracy, 99.73% specificity, 99.43% sensitivity, and 0.996 AUC for the 30,400 thermal images employed. Using the proposed system, 15,159 of 15,200 thermograms belonging to healthy premature babies were classified as healthy, whereas 15,114 of 15,200 thermograms of premature babies, diagnosed with at least one disease, were determined as unhealthy.

1. Introduction

The temperature value of the body is vitally important for health and has been used in medical applications since 400 BC [1]. Healthy skin is characterized by thermal symmetry [2], whereas diseases and infections cause local temperature changes resulting in consequently occurring thermal asymmetry on the skin surface. Hence, temperature measurement devices are used to identify any thermal changes and provide information that facilitates the detection and diagnosis of diseases. In conventional methods, the temperature value is obtained via sensors and electrodes. In all aforementioned materials, the absolute zero point (0 K) emits infrared radiation, and thermal cameras convert the infrared radiation into electrical signals [3,4]. These electrical signals are then converted into thermograms, developed by a processing unit, that include both temperature values and thermal representation. Thermograms have been widely used in various environmental [5], industrial [6], and medical [7] studies. Thermal imaging is called Infrared Thermography (IRT) in medicine. IRT, which is a non-invasive and non-contact method, has been used in medical studies in the fields of thermoregulation [8], breast cancer detection [9,10], neonatal monitoring [11], urology [12,13], and vascular diseases [14,15].

With the development of machine learning algorithms, the application of automatic analyzes such as anomaly detection and lesion segmentation instead of conventional template operations has considerably increased. Therefore, feature engineering methods, including feature extraction [16] and feature selection [17] are becoming increasingly important. Object detection [18], pattern recognition [19,20], medical image classification [21,22], and image segmentation [23,24] have been effectively implemented.

The late diagnosis of diseases and anomalies increases mortality rates. According to statistics of the World Bank [25], the mortality rate in neonates was 18 in 2017. Pre-diagnosis and follow-up treatment systems can be designed by observing the temperature distribution of the skin, and the obtained information can be provided to medical teams. Frequently, the temperature detection and analysis in neonates is performed by electrodes and sensors attached to their sensitive skin

* Corresponding author.
E-mail addresses: mceylan@ktun.edu.tr (M. Ceylan), saim.ervural@karatay.edu.tr (S. Ervural).

https://doi.org/10.1016/j.infrared.2019.103044
Received 2 May 2019; Received in revised form 19 September 2019; Accepted 20 September 2019
Available online 30 September 2019

[26]. In comparison to the use of sensors and electrodes, IRT provides more capabilities, such as monitoring of the heart and respiratory rates, as well as sleeplessness and restlessness.

The first study on neonatal IRT was conducted by Clark and Stothers in 1980. They observed the skin temperature distribution of neonates using thermography and a thermocouple thermometer [11]. A mean square error of 0.107 was obtained in that investigation. In 2012, Abbas et al. proposed compensation techniques for different clinical scenarios, such as convective incubators, kangaroo care, and open radiant warmers [27]. Then, in 2013, Ruqia performed abdominal thermal symmetry analysis for early diagnosis of neonates with necrotizing enterocolitis (NEC) disease [28]. The results of this earlier study showed a higher degree of thermal asymmetry in the group with NEC than in the normal group.

Later, in 2014, Abbas and Leonhardt reported the preliminary results of their feature analysis and Newborn Infrared Thermography (NIRT) imaging [29]. The authors performed decomposition of NIRT images based on independent component analysis and computed the first- and second-order statistical parameters. They also proposed intelligent neonatal monitoring [30]. Skin temperatures of neonates were recorded using thermography, and a vector-based active follow-up system was designed by identifying the region of interest. In 2017, Knobel et al. measured the abdominal and foot temperature of neonates using skin thermistors and thermography [31]. In 2018, Savasci and Ceylan presented the first evaluation results of thermal image analysis for NICU [32]. The obtained results showed differences between the thermal symmetry degrees of healthy and unhealthy neonates. Additionally, Ornek et al. conducted thermal approach analysis using wavelet transform with a thermal map and RGB images [33]. They demonstrated the importance of using a thermal map instead of RGB images.

In recent decades deep learning models, such as multilayer perceptron, CNNs, and recurrent neural networks have been rapidly developing. CNN models [34] were found to have high performance in resolving visible [35–41] and thermal [42–48] image-based problems, such as segmentation, classification, and detection.

Despite a large number of studies on deep learning and thermal imaging, no report related to neonates is available in the literature. Therefore, to the best of our knowledge, this is the first study on the detection of the health status of neonates as healthy and unhealthy by IRT and CNNs.

The rest of the paper is organized as follows. In Section 2, measurement setup and data are presented. In Section 3, methods such as networks architecture, data augmentation, evaluation metrics, and cross-validation are described. Section 4present the detailed results and the subsequent section describes the conclusion.

2. Measurement setup and data

Neonatal thermal images were taken in Selcuk University, Faculty of medicine, NICU over a one-year period. The measurement setup implemented is illustrated in Fig. 1.

Thermal images were obtained using IRBIS, designed by Infratec© Vario- cam HD infrared camera, which is a product of Infratec, was used for the recording of neonatal thermal images. The temperature resolution of the thermal camera is up to 0.02 K at 30 Celcius and the measurement accuracy ± 1 Celcius or ± 1%, the resolution 640 × 480, and hundreds of frames could be captured per second.

Since the temperature distribution of the body skin is so sensitive, the conditions of the imaging room are very important. Therefore, thermal imaging was implemented in thermally controlled NICU and there was set about 25.5 Celcius. Before each measurement, a nurse undressed the neonate, and images were taken from a distance of 60 cm from the incubator. Maintaining the neonate's comfort was critically important, and thus all processes and manipulations were quickly performed. If the image acquisition took more than a minute, the body

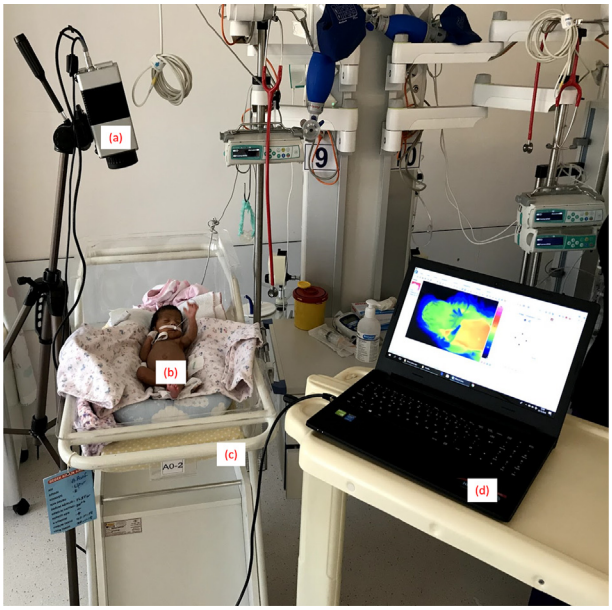

Fig. 1. Measurement Setup (a) infrared camera (b) baby (c) incubator (d) portable computer.

temperature of the neonate decreased, and hypothermia [49] could occur. Five randomly selected neonatal thermal images are displayed in Fig. 2.

The gestational age at the time of delivery of the healthy neonates was from 24 to 34 weeks; their birth weights were between 720 and 2800 g (Table 1).

Of the 19 unhealthy neonates, 10 had one disease, and the other 9 suffered from two diseases. As represented in Table 2, the gestational age of the unhealthy neonates were between 28 and 39 weeks, and their birth weights ranged from 565 to 3300 g.

3. Methods

In the succeeding subsections, we describe the data augmentation for the thermal images, the architecture of the proposed CNN model, the evaluation metrics, and cross-validation. The block diagram of the proposed system is illustrated in Fig. 3. Data augmentation methods were implemented using MATLAB. The development of the CNNs model and the classification were accomplished by PYTHON and Keras library which uses TensorFlow backend. All the process was run on Nvidia Quadro K2200 4 GB 128 Bit 640 Cuda GPU.

Image acquisition was performed, and 100 neonatal thermal images were obtained from each neonate, which were augmented into 800 thermal images. In the first approach, 10 images were selected from each group of 100 images taken from each neonate, or a total number of 380 images were used for the classification task. In the second approach, all of the 100 images of each neonate were employed, and a total number of 3800 images were provided for the classification task. In the third and fourth approaches, each group of 100 images was augmented into 400 and then 800 images, respectively. The total number of images used for the classification task was 15,200 and 30,400, respectively.

3.1. Data augmentation for thermal images

Obtaining neonatal thermal images was difficult due to the conditions in the NICU and neonates. For example, since thermal cameras detect the infrared radiation emitted from the surface, in our case, the skin, neonate had to be undressed. However, some neonates had surgical dressing and since it was not possible to remove these surgical

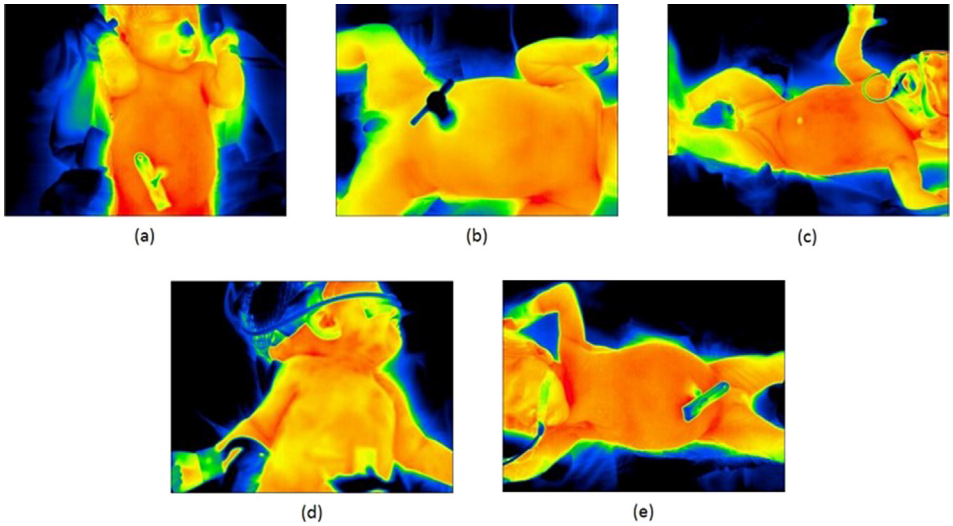

Fig. 2. Randomly selected neonatal thermal images.

Table 1
Physical characteristics of healthy neonates.

Subject	Birth weight (g)	Gestational age in weeks + day
Healthy_1	720	24
Healthy_2	1825	34
Healthy_3	1300	28
Healthy_4	1100	28
Healthy_5	1375	28 + 2
Healthy_6	2200	32
Healthy_7	1580	29
Healthy_8	1690	30 + 5
Healthy_9	955	27
Healthy_10	1175	28 + 4
Healthy_11	1870	31 + 6
Healthy_12	1900	32 + 5
Healthy_13	2300	33 + 5
Healthy_14	1195	29 + 3
Healthy_15	950	28 + 5
Healthy_16	2800	35
Healthy_17	1605	33 + 6
Healthy_18	1885	32 + 1
Healthy_19	1660	32 + 1

dressing, every neonate's thermal image could be taken. On the other hand, the used HD infrared thermal camera takes a hundred frames per second. The body temperature of neonates must be protected. Therefore, the image acquisition should not have taken more than a minute, otherwise, hypothermia could have occurred.

A higher number of images are necessary for the effective training of CNN models. Data augmentation is a method used to create new data with states different from those of the original data. Brightness enhancement, resolution, and contrast changes, as well as the addition of three different noises and color transformation, were utilized as data augmentation methods according to [50]. Thus, the neonatal thermal images were sevenfold augmented (Fig. 4).

The range of the pixel values of the original image in Fig. 4(a) is between 0 and 1. To enhance the brightness of the image, 0.3 was added to all pixels and values greater than 1 were equated to 1. Thus, the range of pixel values was mapped between 0.3 and 1, the obtained image is shown in Fig. 4(b). To change images contrast, all pixels were multiplied by 0.5, in other words, the values of all pixels were reduced to half, thus the darker images were obtained as shown in Fig. 4(c). To reduce the resolution, the size of images has remained the same and the resolution was reduced by a quarter, the obtained image is shown in Fig. 4(d). The images were separated into red, green, and blue bands and then reconstructed from red, green, and green bands for color

Table 2
Physical characteristics of unhealthy neonates.

Subject	Birth weight (g)	Gestational age in weeks + day	Disease 1	Disease 2
Unhealthy_1	2015	34	IKK	Hypothermia
Unhealthy_2	1100	28	Respiratory distress	–
Unhealthy_3	3300	33 + 1	RDS	–
Unhealthy_4	3000	36	NEC	PDA
Unhealthy_5	865	28	Respiratory distress	Moaning
Unhealthy_6	1890	33 + 2	Respiratory distress	DAB
Unhealthy_7	2055	34	PAB	–
Unhealthy_8	1985	32	NEC	–
Unhealthy_9	2305	34 + 1	Intestinal obstruction	–
Unhealthy_10	2280	37	Hypoplastic left heart	–
Unhealthy_11	2200	35	Ozofagus atrezi	–
Unhealthy_12	1590	30	Respiratory distress	Neonatal syphilis
Unhealthy_13	1790	31	NEC	Sepsis
Unhealthy_14	2680	38	Diaphragm hernia	Adeno
Unhealthy_15	2700	35	TTN	–
Unhealthy_16	565	28	IUGR	–
Unhealthy_17	3079	37	Ozofagus atrezi	–
Unhealthy_18	3300	38	Hydrocephalus	Myelomen- ingocele
Unhealthy_19	1100	33	AORT coarctation	Down syndrome

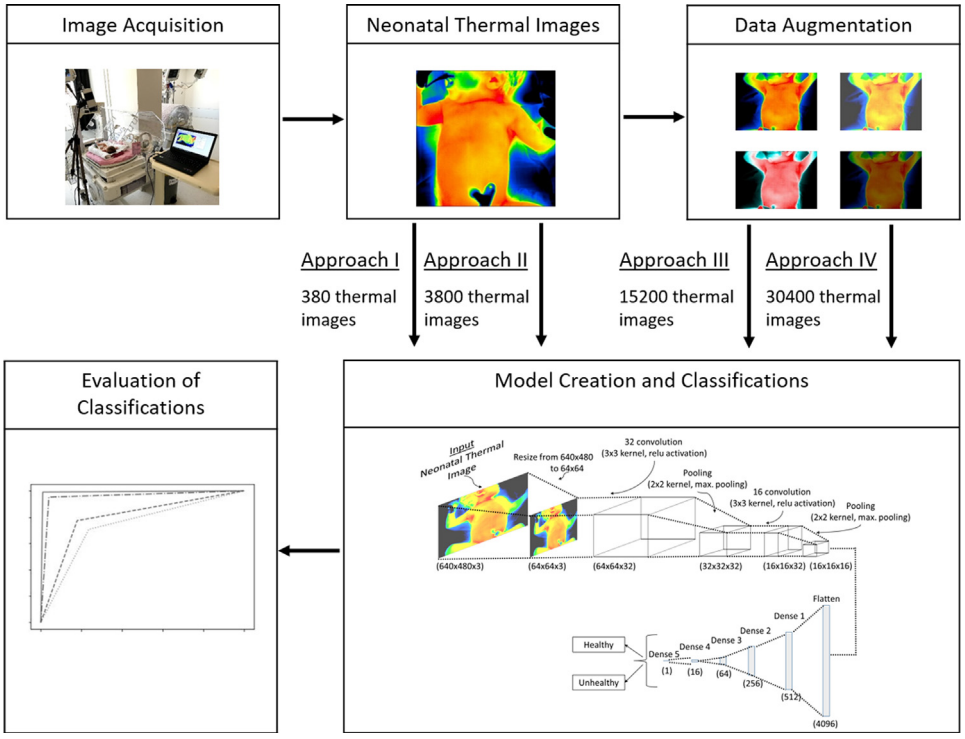

Fig. 3. Block Diagram of the proposed system.

transformation. Thus, the blue band was removed from the images, which transformed the color of the images, as depicted in Fig. 4(e). Also, the obtained thermal image is similar to the images obtained by visible imaging. During the process of obtaining the images, the systems had to be resistant to drifting in the temperature distribution. To model the drifting, salt and pepper noises with different densities (0.01, 0.02, and 0.08) were added to the images Fig. 4(f–h).

3.2. The network architecture

CNN model is a deep learning model that provides high image performance and is – based on applications, such as object detection, pattern recognition, image segmentation, and classification [34].

CNN models consist of two main layers: convolutional and fully connected. The convolutional layer includes convolution and pooling operations. Convolution operation represents the extraction of the features of the image depending on the selected kernel. The dimensions of the kernel can be selected as 3 × 3, 5 × 5, or 7 × 7. Pooling operation refers to the reduction in the dimensions of the obtained feature map according to pooling size and selected methods such as average and maximum pooling. In this study, the convolution kernel size was selected as 3 × 3, and the maximum pooling kernel size as 2 × 2.

The fully connected layer consists of flattening operation and dense layers. The flatten operation converts the obtained feature maps into a feature vector. Subsequently, the dense layer creates weights to classify the obtained vector. The architecture of our CNN model is illustrated in Fig. 5.

Activation functions were used to set the output values. The rectified linear unit (relu) activation function [51] converts the input values (a) to f (a) = max (0, a). On the other hand, the sigmoid activation function [52] converts the input value (a) to f (a) = 1/(1 + e-a), which is a value between 0 and 1.

As can be seen in Fig. 5, our proposed CNN model included two convolutional, two pooling, one flatten, and five dense layers. We resized the dimensions of the input images from 512 × 512 to 64 × 64. The first convolutional layer consisted of 32 different 3 × 3 dimensional layers (activation function = relu), whereas the second convolutional layer contained 16 different 3 × 3 dimensional layers

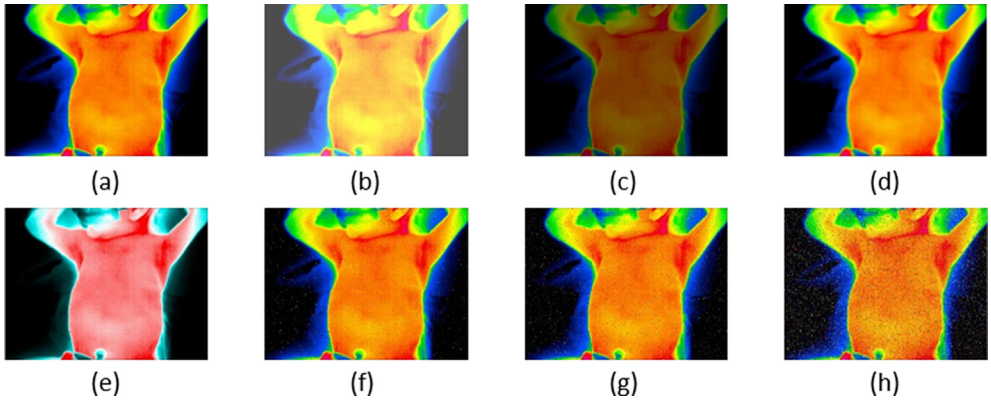

Fig. 4. Augmented thermal images (a) original (b) brightness enhancement (c) contrast changing (d) resolution changing (e) color transforming (f–h) salt and pepper noise adding with 0.01, 0.02 and 0.08 densities, respectively.

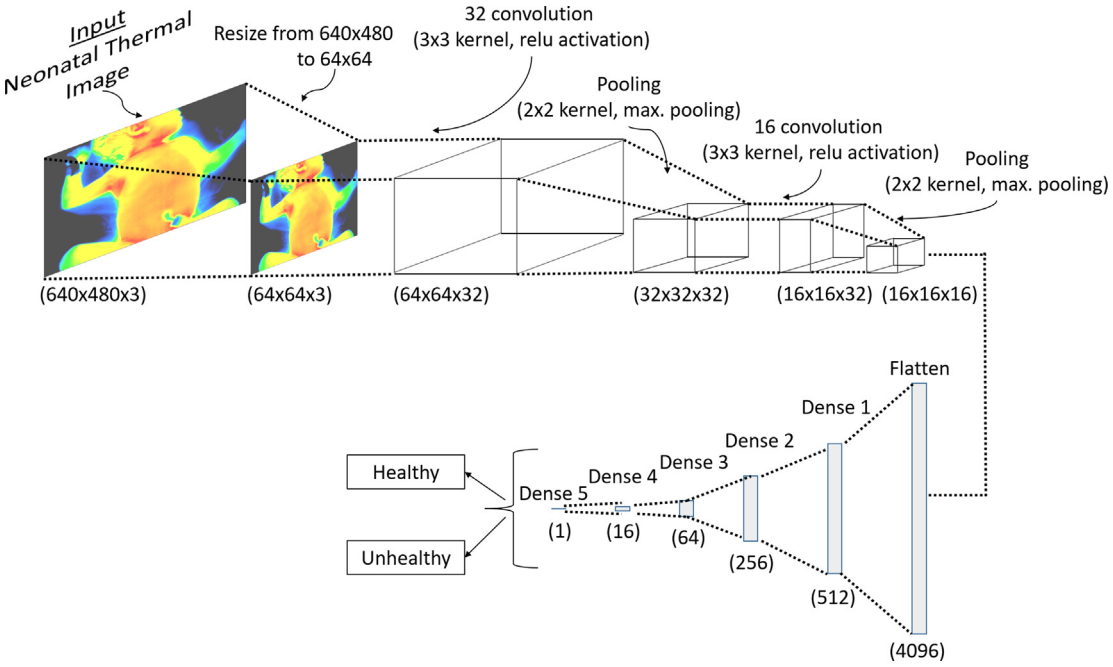

Fig. 5. Proposed convolutional neural networks model.

(activation function = relu). The dimensions of the two used pooling layers were 2 × 2 (pooling = max pooling). The first four dense layers consisted of 512, 256, 64, and 16 neurons, respectively (activation function = relu), and the fifth layer, called the output layer, included one neuron (activation function = sigmoid). The output values varied from 0 to 1. If the obtained value was bigger than 0.5, it was classified as unhealthy and if the obtained value was lower than or equal to 0.5, it was categorized as healthy.

The training parameters of the model were empirically defined. The number of training epochs was selected as 3, and the samples number per epoch was selected as 2000. The optimizer and loss function was selected as Adam [53] and binary cross-entropy [54], respectively.

3.3. Evaluation metrics

To evaluate the performance of the classification, the confusion matrix, sensitivity (1), specificity (2), and accuracy (3) values were calculated [55]. The confusion matrix represents the number of true positives (TPs), true negatives (TNs), false positives (FPs), and false negatives (FNs) (Fig. 6). Where TP represents the number of unhealthy neonates labeled as unhealthy while TN is the number of healthy neonates labeled as healthy. In addition, FP represents the number of healthy neonates labeled as unhealthy, and FN is the number of unhealthy neonates labeled as healthy.

$$Sensitivity = \frac{TP}{TP + FN} \quad (1)$$

$$Specificity = \frac{TN}{TN + FP} \quad (2)$$

$$Accuracy = \frac{(TP + TN)}{(TN + TP + FN + FP)} \quad (3)$$

The operating characteristic (ROC) curve and area under the curve (AUC) value have been calculated to compare the realized classifications [56]. ROC curve was constructed using the TP and FP rates. The AUC value corresponds to the possibility of the obtained results. The AUC value was between 0 and 1; AUC = 1 indicated the optimal classification result.

	Estimated Class	
Real Class	TP	FN
	FP	TN

Fig. 6. Confusion matrix representation.

3.4. Cross-validation

Data were frequently split into fixed testing and training parts to evaluate the metrics obtained from the classification. Since a specific part of the data was used in this method, it was inadequate for the evaluation of the results. K-fold cross-validation [57] is a method that is used for calculations of the reliability of the evaluation metrics of the created model. According to the k-fold cross-validation, the data were split into K parts, and each unit of datum was set as testing and training data. In this study, K value was selected as 10 and the data are split into 10 parts. The number of testing and training data is shown in Table 3.

As can be seen from Table 3, four different approaches were realized. In the first approach, 10 images were taken from each one of the 38 neonates; this way, 380 images were used. According to the 10-fold cross-validation performed, 380 thermal images were split into 10 parts. Hence, 38 images were defined as the testing set, and the remaining 342 images were classified as the training set. Furthermore, another 38 images were reserved for the testing. This way, all images were used for both testing and training. As a result, 10 different confusion matrices were obtained. After the completion of 10–fold cross-validation, 10 confusion matrices were summed, and the evaluation metrics were calculated. In the second approach, 3800 neonatal thermal images were selected, of which380 images were used for testing and 3420 for training. After data augmentation was

Table 3
Number of training and testing data.

Approach	Total	Training	Testing
I	380	342	38
II	3800	3420	380
III	15,200	13,680	1520
IV	30,400	27,360	3040

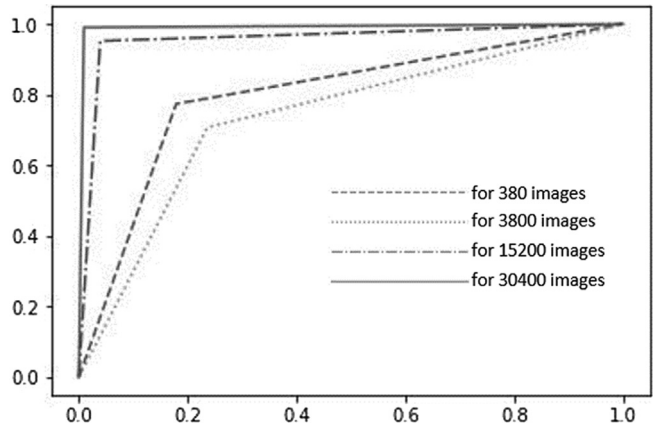

Fig. 7. Confusion matrix representation.

implemented, 400 neonatal thermal images taken from every neonate were used in the third approach, totaling a number of 15,200 images obtained. Using 10-fold cross-validation, 1520 images were utilized for testing and 13,680 images for training. In the fourth approach, 800 images of every neonate were obtained, that is 30,400 images, 3040 of which were for testing and 27,360 for ten-fold training.

4. Results

In this study 380, 3800, 15,200, and 30,400 thermal images belonged to 38 neonates that were classified as healthy and unhealthy. Confusion matrices were calculated using a 10 – fold cross-validation method. Sensitivity, specificity and accuracy metrics were obtained from confusion matrices and these metrics were used to evaluate the performance of classification. The obtained ROC curve is depicted in Fig. 7 and all results are presented in Table 4.

We used 380 thermal images by taking 10 different images from every neonate in approach I. As can be seen from Table 4, of the 190 unhealthy thermal images, 156 were classified as unhealthy, and of the 190 healthy thermal images, 147 were categorized as healthy. The evaluation metrics of approach I results were obtained as 82.10% sensitivity, 77.36% specificity, 79.73% accuracy, and 0.797 AUC.

When the number of the thermal images was increased from 380 to 3800, all evaluation metrics values of approach II results were decreased. For example, the accuracy and AUC metrics diminished from 79.73% and 0.797 to 70.73 and 0.736, correspondingly. Augmentation of the original thermal data was not implemented until the application of approach III. All used data were selected from the original thermal images.

Data augmentation methods, such as brightness enhancement, contrast changing, and salt and pepper noise addition at a density of 0.02 were implemented in approach III. That is the original thermal images were threefold augmented. Thus, the CNN model was trained with 15,200 thermal images (11,400 augmented, 3800 original). As can be seen from Table 4, the sensitivity, specificity, and accuracy metrics of approach III are above 99%, and AUC is 0.991.

In approach IV, new data augmentation methods, such as resolution changes, color transformation, and two different salt and pepper noise additions at densities of 0.01 and 0.08 were added. Thus, new 15,200 augmented thermal images were obtained, and totally 30,400 thermal images were used in the training of the CNN model.

The optimal results were obtained in this approach. Of the 15,200 unhealthy thermal images, 15,159 were classified as unhealthy and of the 15,200 healthy thermal images, 15,114 as healthy. The best sensitivity obtained was 99.73%, specificity was obtained as 99.43%, accuracy was obtained as 99.58% and AUC was obtained as 0.996.

Table 4
Results table.

Approach	Confusion Matrix		Sensitivity	Specificity	Accuracy	AUC
I	156	34	82.10%	77.36%	79.73%	0.797
	43	147				
II	1451	449	76.36%	70.73%	73.55%	0.736
	556	1344				
III	7529	71	99.06%	99.07%	99.07%	0.991
	70	7530				
IV	15,159	41	99.73%	99.43%	99.58%	0.996
	86	15,114				

5. Discussion and conclusions

Thermal imaging which is a non-contact and non-invasive method provides more capabilities than visible imaging. For example, temperature values of the body can be obtained with thermal imaging even in darkness. Thermal imaging applications are called Infrared Thermography (IRT) in medicine. Body temperature is considerably important for health status evaluations, and since diseases, disorders and infections cause thermal anomalies over the body, IRT can be used to detect breast cancer and vascular diseases and realize neonatal monitoring systems.

For the last four decades, studies on neonatal IRT have been consistently pursued. Frequently, methods such as region of interest selection, specific template creating and matching over the body and comparison of reference have been used. But, these methods contain a lot of specific operations and they are not always valid. Since neonates move right to left in an incubator, created specific templates do not match for every movement.

Problems that cannot be solved using the classic methods have been rapidly solved with the developing of deep learning methods in recent decades. Especially deep Convolutional Neural Networks (CNNs) models demonstrate high performance at solving both visible and thermal images-based problems such as classification, detection and segmentation. In CNNs models, feature extraction and reduction, region of interest selection and specific code creation are not realized. The user creates a CNNs model architecture with convolutional and fully – connected layers and this model creates codes and solves problems itself.

Until this study, CNNs models were not used for neonatal IRT. We collected thermal images of neonates in Selcuk University, Faculty of Medicine, Neonatal Intensive Care Unit for a year. Here, we used neonatal images taken of 38 different neonates (19 healthy and 19 unhealthy).

The neonates tended to move while thermal images were being taken, which reduced the performance of the conventional neonatal monitoring methods. Since our created CNN model is trained with images taken in different positions during the movements of the neonates, it does not affect the model's performance.

The only problem that the CNN model may face is the lack of data. We used data augmentation methods to overcome this issue. Brightness enhancement, contrast, and resolution changes, color transformation, and noises additions were implemented to the acquired thermal images. Thus, we trained our CNNs model with 380, 3800, 15,200, and 30,400 thermal images. The best results obtained were: 99.73% sensitivity, 99.43% specificity, 99.58% accuracy, and 0.996 AUC for the healthy and unhealthy classification of neonates by using 30,400 images.

In future studies, we aim to create a pre-diagnosis system to detect diseases, such as respiratory distress syndrome, patent ductus arteriosus, necrotizing enterocolitis, and congenital diaphragmatic hernia. Further improvement of the findings and approaches employed in this study will facilitate the development of a system with the potential to follow up and monitor the daily status and treatment process of neonates. Therefore, these advancements can decrease the mortality rates of neonates in cases when the problems that occur have been earlier

reported to doctors.

Declaration of Competing Interest

The authors declared that there is no conflict of interest.

Acknowledgments

This study was supported by the Scientific and Technological Research Council of Turkey (TUBITAK, project number: 215E019). The authors express their gratitude to Selcuk University's expert pediatricians H. Soylu and M. Konak, for their help and future vision. We also thank all the staff who helped during the process of taking thermal images of the neonates in the neonatal intensive care unit.

Appendix A. Supplementary material

Supplementary data associated with this article can be found, in the online version, at https://doi.org/10.1016/j.infrared.2019.103044.

References

[1] B.B. Lahiri, S. Bagavathiappan, T. Jayakumar, et al., Medical applications of infrared thermography: a review, Infrared Phys. Technol. 55 (4) (2012) 221–235.
[2] R. Dail, B. Guenther, H.E. Rice, Thermoregulation and Thermography in Neonatal Physiology and Disease, 2011.
[3] G. Jagannathan, A Case for Joint Development of IR Cameras in India, 2007.
[4] C. Hildebrandt, K. Zeilberger, E.F.J. Ring, et al., The Application of Medical Infrared Thermography in Sports Medicine, 2012.
[5] Y. Ohashi, I. Uchida, Applying dynamic thermography in the diagnosis of breast cancer, IEEE Eng. Med. Biol. Mag. 19 (3) (2000) 42–51.
[6] R. Usamentiaga, D.F. García, J. Molleda, et al., Temperature tracking system for sinter material in a rotatory cooler based on infrared thermography, IEEE Trans. Ind. Appl. 50 (5) (2014) 3095–3102.
[7] F. Bisegna, D. Ambrosini, IR thermography as a preliminary tool in acoustical inspection of ancient historical structures, pp. 1–4.
[8] T.S. Kammersgaard, J. Malmkvist, L.J. Pedersen, Infrared thermography – a noninvasive tool to evaluate thermal status of neonatal pigs based on surface temperature, Animal 7 (12) (2013) 2026–2034.
[9] N. Arora, D. Martins, D. Ruggerio, et al., Effectiveness of a noninvasive digital infrared thermal imaging system in the detection of breast cancer, Am. J. Surg. 196 (4) (2008) 523–526.
[10] M. Kontos, R. Wilson, I. Fentiman, Digital infrared thermal imaging (DITI) of breast lesions: sensitivity and specificity of detection of primary breast cancers, Clin. Radiol. 66 (6) (2011) 536–539.
[11] R.P. Clark, J.K. Stothers, Neonatal skin temperature distribution using infra-red colour thermography, J. Physiol. 302 (1980) 323–333.
[12] A.R. Zlotta, S.D. Edwards, C.C. Schulman, et al., Transurethral Needle Ablation (TUNA): thermal gradient mapping and comparison of lesion size in a tissue model and in patients with benign prostatic hyperplasia, Eur. Urol. 24 (1993) 411–414.
[13] W. Kee Ng, E. Ng, Y. Tan, Qualitative Study of Sexual Functioning in Couples with Erectile Dysfunction Prospective Evaluation of the Thermography Diagnostic System, 2009.
[14] S. Bagavathiappan, T. Saravanan, J. Philip, et al., "Investigation of peripheral vascular disorders using thermal imaging, Br. J. Diabetes Vasc. Dis. 8 (2) (2008) 102–104.
[15] S. Bagavathiappan, T. Saravanan, J. Philip, et al., Infrared thermal imaging for detection of peripheral vascular disorders, J. Med. Phys. 34 (1) (2009) 43–47.
[16] H. Yaşar, M. Ceylan, A new method for extraction of image's features: Complex discrete Ripplet-II transform, pp. 1673–1676.
[17] T. Ojala, M. Pietikainen, T. Maenpaa, Multiresolution gray-scale and rotation invariant texture classification with local binary patterns, IEEE Trans. Pattern Anal. Mach. Intell. 24 (7) (2002) 971–987.
[18] F. Azadi Pourghahestani, E. Rashedi, Object detection in images using artificial neural network and improved binary gravitational search algorithm, 2015.
[19] R.S.H. Mah, V. Chakravarthy, Pattern recognition using artificial neural networks, Comput. Chem. Eng. 16 (4) (1992) 371–377.
[20] T.-H. Kim, Pattern Recognition Using Artificial Neural Network: A Review, pp. 138–148.
[21] M. Singh, S. Singh, S. Gupta, An information fusion based method for liver classification using texture analysis of ultrasound images, Inform. Fusion 19 (2014) 91–96.
[22] A.E. Canbilen, M. Ceylan, A novel approach for the classification of liver MR images using complex orthogonal ripplet-II and wavelet-based transforms, classification in BioApps: automation of decision making, in: N. Dey, A.S. Ashour, S. Borra (Eds.), Springer International Publishing, Cham, 2018, pp. 33–56.
[23] M. Ceylan, Y. Özbay, E. Yıldırım, A new approach for biomedical image segmentation: Combined complex-valued artificial neural network case study: Lung segmentation on chest CT images, pp. 33–36.
[24] N. Lanisa, N. Siew Cheok, L. Kw, Color morphology and segmentation of the breast thermography image, 2015.
[25] W.B. Group. Mortality rate, neonatal (per 1,000 live births), https://data.worldbank.org/indicator/SH.DYN.NMRT?end=2017&start=1990&view=chart.
[26] Y. Ethawi, A.K. Abbas, M. Narvey, et al., Review of Biomedical Applications of Contactless Imaging of Neonates Using Infrared Thermography and Beyond, 2018.
[27] A.K. Abbas, K. Heimann, V. Blazek, et al., Neonatal infrared thermography imaging: analysis of heat flux during different clinical scenarios, Infrared Phys. Technol. 55 (6) (2012) 538–548.
[28] R. Nur, Identification of Thermal Abnormalities by Analysis of Abdominal Infrared Thermal Images of Neonatal Patients, 2013.
[29] A.K. Abbas, S. Leonhardt, Neonatal IR-Thermography Pattern Clustering based on ICA Algorithm, 2014.
[30] A.K. Abbas, S. Leonhardt, Intelligent neonatal monitoring based on a virtual thermal sensor, BMC Med. Imag. 14 (2014) 9.
[31] R.B. Knobel-Dail, D. Holditch-Davis, R. Sloane, et al., Body temperature in premature infants during the first week of life: exploration using infrared thermal imaging, J. Therm. Biol. 69 (2017) 118–123.
[32] D. Savaşci, M. Ceylan, Thermal image analysis for neonatal intensive care units (First evaluation results), pp. 1–4.
[33] A.H. Ornek, D. Savasci, M. Ceylan, et al., Determination of correct approaches in evaluation of thermograms, in: URSI-TURKIYE IX. Scientific Congress, 2018.
[34] A. Krizhevsky, I. Sutskever, G.E. Hinton, ImageNet classification with deep convolutional neural networks, in: Proceedings of the 25th International Conference on Neural Information Processing Systems, Lake Tahoe, Nevada, vol. 1, 2012, pp. 1097–1105.
[35] P. Sermanet, S. Chintala, Y. LeCun, Convolutional neural networks applied to house numbers digit classification, pp. 3288–3291.
[36] M. Mazumdar, V. Sarasvathi, A. Kumar, Object recognition in videos by sequential frame extraction using convolutional neural networks and fully connected neural networks, pp. 1485–1488.
[37] R. Shimizu, S. Yanagawa, T. Shimizu, et al., Convolutional neural network for industrial egg classification, pp. 67–68.
[38] S. Kumar, A. Tyagi, T. Sahu, et al., Indian Art Form Recognition Using Convolutional Neural Networks, pp. 800–804.
[39] D. Lim, H. Kim, S. Hong, et al., Practically Classifying Unmanned Aerial Vehicles Sound Using Convolutional Neural Networks, pp. 242–245.
[40] J. Rathod, V. Wazhmode, A. Sodha, et al., Diagnosis of skin diseases using Convolutional Neural Networks. pp. 1048–1051.
[41] L. Zhang, Z. Chen, B. Zou, et al., Polarimetric SAR Terrain Classification Using 3D Convolutional Neural Network. pp. 4551–4554.
[42] E. Gundogdu, A. Koç, A.A. Alatan, Object classification in infrared images using deep representations. pp. 1066–1070.
[43] Y. Cho, N. Bianchi-Berthouze, S.J. Julier, DeepBreath: deep learning of breathing patterns for automatic stress recognition using low-cost thermal imaging in unconstrained settings, pp. 456–463.
[44] C. Lile, L. Yiqun, Anomaly detection in thermal images using deep neural networks, pp. 2299–2303.
[45] M.B. Lopez, C.R. del-Blanco, N. Garcia, Detecting exercise-induced fatigue using thermal imaging and deep learning. pp. 1–6.
[46] Y. Cho, N. Bianchi-Berthouze, N. Marquardt, et al., Deep thermal imaging: proximate material type recognition in the wild through deep learning of spatial surface temperature patterns, in: Proceedings of the 2018 CHI Conference on Human Factors in Computing Systems, Montreal QC, Canada, 2018, pp. 1–13.
[47] O. Janssens, R.V.d. Walle, M. Loccufier, et al., Deep learning for infrared thermal image based machine health monitoring, IEEE/ASME Trans. Mechatron. 23 (1) (2018) 151–159.
[48] M.Z. Uddin, J. Torresen, A Deep Learning-Based Human Activity Recognition in Darkness. pp. 1–5.
[49] D.J.A. Brown, H. Brugger, J. Boyd, et al., Accidental hypothermia, N. Engl. J. Med. 367 (20) (2012) 1930–1938.
[50] A.H. Ornek, M. Ceylan, Comparison of Traditional Transformations for Data Augmentation in Deep Learning of Medical Thermography, 2019.
[51] V. Nair, G.E. Hinton, Rectified Linear Units Improve Restricted Boltzmann Machines Vinod Nair, 2010.
[52] S. Narayan, The generalized sigmoid activation function: competitive supervised learning, Inf. Sci. 99 (1) (1997) 69–82.
[53] D. Kingma, J. Ba, Adam: A Method for Stochastic Optimization, 2014.
[54] J. Shore, R. Johnson, Axiomatic derivation of the principle of maximum entropy and the principle of minimum cross-entropy, IEEE Trans. Inf. Theory 26 (1) (1980) 26–37.
[55] W. Zhu, N. Zeng, N. Wang, Sensitivity, specificity, accuracy, associated confidence interval and ROC analysis with practical SAS implementations, NESUG Proceedings: Health Care and Life Sciences, Baltimore, Maryland, 2010, p. 67.
[56] J.A. Hanley, B.J. McNeil, The meaning and use of the area under a receiver operating characteristic (ROC) curve, Radiology 143 (1) (1982) 29–36.
[57] R. Kohavi, A Study of Cross-Validation and Bootstrap for Accuracy Estimation and Model Selection, 2001.